AMERICAN SOCIETY FOR MICROBIOLOGY | Antimicrobial Agents and Chemotherapy®

MECHANISMS OF ACTION: PHYSIOLOGICAL EFFECTS

Cryo-Electron Microscopy Structure of the *Mycobacterium tuberculosis* Cytochrome *bcc:aa*$_3$ Supercomplex and a Novel Inhibitor Targeting Subunit Cytochrome *c*I

Vikneswaran Mathiyazakan,[a,b] **Chui-Fann Wong,**[b] **Amaravadhi Harikishore,**[b] **Kevin Pethe,**[a,b] **Gerhard Grüber**[b]

[a]Lee Kong Chian School of Medicine, Nanyang Technological University, Singapore, Republic of Singapore
[b]Nanyang Technological University, School of Biological Sciences, Singapore, Republic of Singapore

ABSTRACT The mycobacterial cytochrome *bcc:aa*$_3$ complex deserves the name "supercomplex" since it combines three cytochrome oxidases—cytochrome *bc*, cytochrome *c*, and cytochrome *aa*$_3$—into one supramolecular machine and performs electron transfer for the reduction of oxygen to water and proton transport to generate the proton motive force for ATP synthesis. Thus, the *bcc:aa*$_3$ complex represents a valid drug target for *Mycobacterium tuberculosis* infections. The production and purification of an entire *M. tuberculosis* cytochrome *bcc:aa*$_3$ are fundamental for biochemical and structural characterization of this supercomplex, paving the way for new inhibitor targets and molecules. Here, we produced and purified the entire and active *M. tuberculosis* cyt-*bcc:aa*$_3$ oxidase, as demonstrated by the different heme spectra and an oxygen consumption assay. The resolved *M. tuberculosis* cyt-*bcc:aa*$_3$ cryo-electron microscopy structure reveals a dimer with its functional domains involved in electron, proton, oxygen transfer, and oxygen reduction. The structure shows the two cytochrome *c*I*c*II head domains of the dimer, the counterpart of the soluble mitochondrial cytochrome *c*, in a so-called "closed state," in which electrons are translocated from the *bcc* to the *aa*$_3$ domain. The structural and mechanistic insights provided the basis for a virtual screening campaign that identified a potent *M. tuberculosis* cyt-*bcc:aa*$_3$ inhibitor, cyt*Mycc*1. cyt*Mycc*1 targets the mycobacterium-specific α3-helix of cytochrome *c*I and interferes with oxygen consumption by interrupting electron translocation via the *c*I*c*II head. The successful identification of a new cyt-*bcc:aa*$_3$ inhibitor demonstrates the potential of a structure-mechanism-based approach for novel compound development.

KEYWORDS cytochrome *bcc:aa*$_3$ oxidase, bioenergetics, OXPHOS, tuberculosis, *Mycobacterium tuberculosis*, inhibitor

The tuberculosis (TB) causing pathogen *Mycobacterium tuberculosis* is an obligate aerobe that is strictly dependent on oxygen to meet its energetics demand during growth. Without any effective fermentative process, the oxidative phosphorylation (OXPHOS) pathway is crucial to maintain redox homeostasis and synthesis of sufficient amount of ATP (Fig. 1) (1, 2). Most mycobacteria contain a proton-pumping cytochrome *bcc:aa*$_3$ oxidase supercomplex (cyt-*bcc:aa*$_3$) and a non-proton-pumping, less energetically efficient, cytochrome *bd* oxidase (cyt-*bd*) (3, 4). The discovery and visualization of the phase 2 candidate Telacebec (Q203), which targets the substrate-binding site of menaquinol of mycobacterial cyt-*bcc:aa*$_3$, validated this complex as a target for anti-TB treatment (5–8).

From an evolutionary perspective, the mycobacterial cyt-*bcc:aa*$_3$ supercomplex is a fusion of the mitochondrial cytochrome *bc* (cyt-*bc*), cytochrome *c*, and cytochrome *aa*$_3$ oxidases (cyt-*aa*$_3$), with cytochrome *c* connecting the electron flow from the substrate quinol in cyt-*bc* oxidase to the cyt-*aa*$_3$ oxidase in which reduction of O_2 to water occurs (9, 10).

Address correspondence to Kevin Pethe, kevin.pethe@ntu.edu.sg, or Gerhard Grüber, ggrueber@ntu.edu.sg.

The authors declare no conflict of interest.

Received 16 November 2022
Returned for modification 16 December 2022
Accepted 30 March 2023
Published 9 May 2023

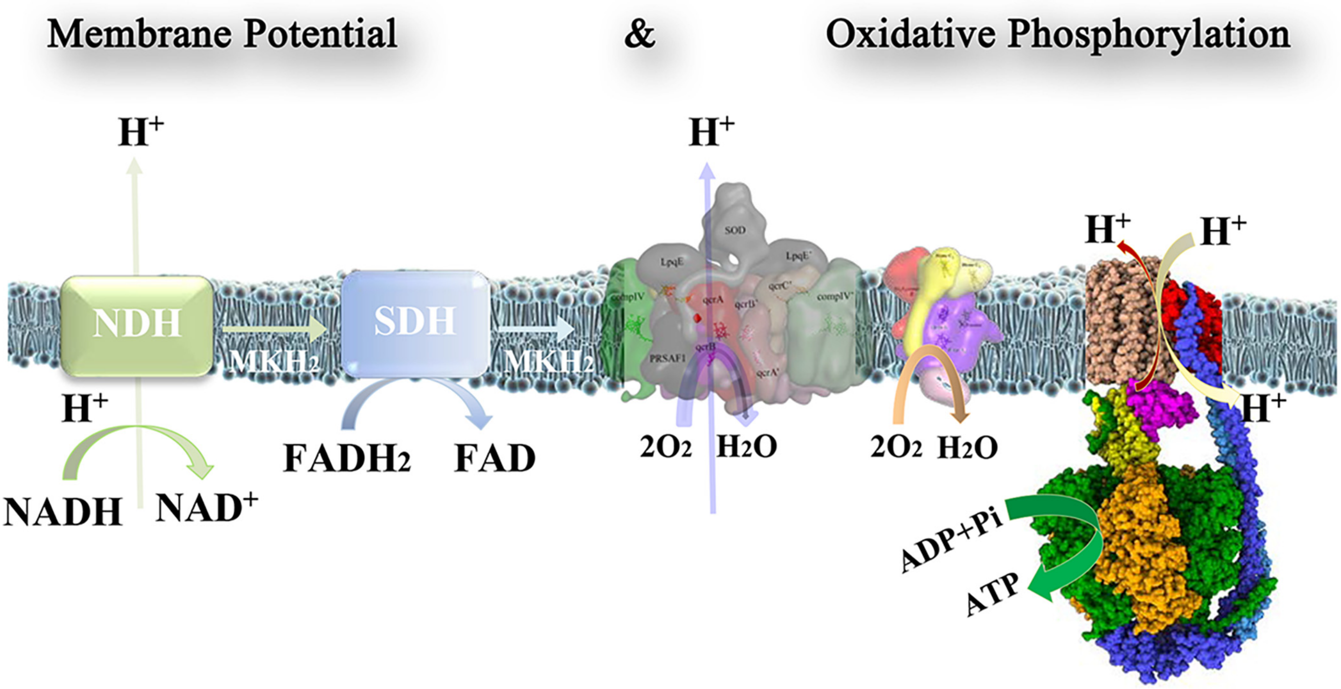

FIG 1 Mycobacterial respiratory chain complexes generate the electrochemical gradient, providing the energy for the formation of ATP by the F_1F_o-ATP synthase. Complexes I (NDH) and II (SDH) oxidize NADH and succinate, respectively. These electrons are transferred to the mycobacterial cyt-*bcc:aa*$_3$ and cyt-*bd* oxidases to reduce oxygen to water. While complex I and the cyt-*bcc:aa*$_3$ pump protons into the intermembrane lumen to generate the proton gradient, the F_o domain of the F_1F_o ATP synthase uses these protons to drive ATP formation in the F_1 domain. The maintenance of a proton gradient and the regulation of ATP production are crucial parameters governing the survival of the bacterium.

The mycobacterial cyt-*bcc* domain consists of subunits QcrC, QcrA, and QcrB, while the cyt-*aa*$_3$ part includes the subunits CtaC and CtaD, relevant for electron transfer and O_2 reduction, as well as the assembly subunits CtaE, CtaF, CtaI, and CtaJ. The mycobacterial subunit QcrC is the counterpart of the mitochondrial cyt-*c*, consisting of a transmembrane helical segment, followed by the two cytochrome *c*I*c*II (cyt-*c*I*c*II) domains, including heme *c*I and *c*II, as demonstrated by the recent cryo-electron microscopy (cryo-EM) structures of the *Mycobacterium smegmatis* cyt-*bcc:aa*$_3$ oxidase (9, 10). The cyt-*c*I*c*II domains are located at the intermembrane space and couple the electron flow from the cyt-*bcc:aa*$_3$ to subunit CtaC of cyt-*aa*$_3$ (1). Mutants of the related *M. smegmatis* lacking subunit CtaC have profoundly impaired growth, indicating the importance of this subunit for bacterial survival and coupling of electrons between cyt-*c*I*c*II and CtaC for the final reduction of oxygen (11).

Understanding the structure, mechanisms, regulation, and *M. tuberculosis*-specific modifications of the cyt-*bcc:aa*$_3$ oxidase requires the isolation of a pure, complete, and enzymatically active *M. tuberculosis* cyt-*bcc:aa*$_3$ oxidase, which is presented here. The first cryo-EM structure of this entire *M. tuberculosis* supercomplex sheds light into the pathways involved in O_2 reduction and the generation of the proton motive force and revealed a mycobacterium-specific epitope essential for electron transfer that we exploited to discover a specific inhibitor.

RESULTS AND DISCUSSION

Expression, production, and purification of the recombinant *M. tuberculosis* cyt-*bcc:aa*$_3$. The expression and production of the membrane-embedded, multisubunit complexes of *M. tuberculosis* represents a challenge (12, 13). Here, we used *M. bovis* BCG as an expression system, a nonpathogenic species in which the cyt-*bcc:aa*$_3$ is 100% homolog to the *M. tuberculosis* counterpart. cyt-*bcc:aa*$_3$ was tagged at the C terminus of subunit QcrB using the ORBIT (oligonucleotide-mediated recombineering,

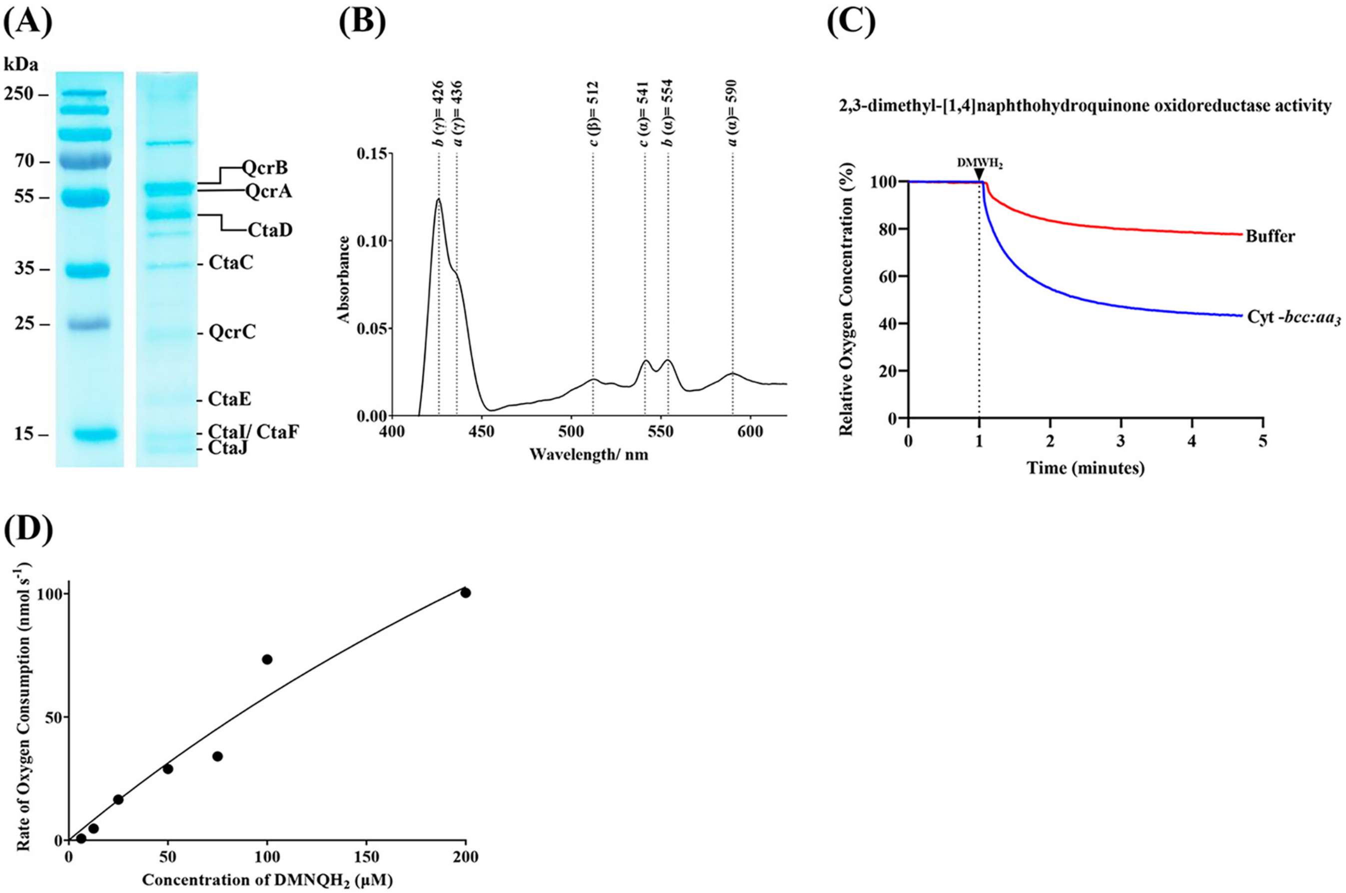

FIG 2 Characterization of purified *M. tuberculosis* cyt-*bcc:aa*$_3$. (A) 12% SDS gel profile of purified supercomplex. The bands for QcrB, QcrA, and QcrC were further confirmed through matrix-assisted laser desorption/ionization-time of flight (MALDI-TOF) mass spectrometry (MS) (see (Table S1A to C in the supplemental material). (B) Difference spectrum of purified *M. tuberculosis* cyt-*bcc:aa*$_3$ after reduction with $Na_2S_2O_4$. The spectrum registered peaks for heme *a* (437 nm, 592 nm), heme *b* (424 nm, 555 nm), and heme *c* (512 nm, 543 nm). (C) Characterization of the purified enzyme in an oxygen consumption assay. In the presence of 2,3-dimethyl[1,4]naphthohydroquinone, the purified supercomplex reduced oxygen levels significantly, as shown by the profile after subtracting background activity. (D) Enzyme kinetics of *M. tuberculosis* cyt-*bcc:aa*$_3$. A dose response of 2,3-dimethyl[1,4]naphthohydroquinone was used to determine the K_m, k_{cat}, and k_{cat}/K_m values of the enzyme.

followed by Bxb1 integrase targeting) technology, as described in Materials and Methods (14).

The *M. tuberculosis* cyt-*bcc:aa*$_3$ was solubilized in a buffer containing 1% (wt/vol) *n*-dodecyl-*β*-D-maltoside (DDM; 20 mM morpholinepropanesulfonic acid [MOPS; pH 7.4], 100 mM NaCl, 2 mM Pefabloc, 1 mM phenylmethylsulfonyl fluoride [PMSF], 1% [wt/vol] DDM, 10% glycerol) by stirring for 1 h at 4°C. Afterward, the mixture was ultracentrifuged (39,500 × *g* for 30 min at 4°C), and the supernatant was incubated with 1 mL of FLAG beads at 4°C for 1 h. To reduce the detergent content and prevent subunit dissociation, the resin was washed with a buffer of lower DDM content (20 mM MOPS [pH 7.4], 100 mM NaCl, 2 mM Pefabloc, 1 mM PMSF, 0.1% [wt/vol] DDM, 5% glycerol). The recombinant *M. tuberculosis* cyt-*bcc:aa*$_3$ was eluted by a buffer including FLAG peptide (20 mM MOPS [pH 7.4], 100 mM NaCl, 2 mM Pefabloc, 1 mM PMSF, 0.1% [wt/vol] DDM, 100 μg/mL of 3× FLAG peptide). SDS-PAGE (Fig. 2A) and MALDI analysis (see Table S1A to C in the supplemental material) revealed that the eluted complex contained the subunits QcrA-C, CtaC, CtaD, CtaE, CtaF, CtaI, and CtaJ.

To prove the electron transfer, *M. tuberculosis* cyt-*bcc:aa*$_3$ was first oxidized by 100 mM potassium ferricyanide ($K_3[Fe(CN)_6]$), followed by the chemical reduction using sodium dithionite ($Na_2S_2O_4$). The respective difference spectrum confirmed that all the hemes—*a*, *b*, and *c*—are within the purified complex and contribute to electron translocation (Fig. 2B). To further test whether the recombinant *M. tuberculosis* cyt-*bcc:aa*$_3$

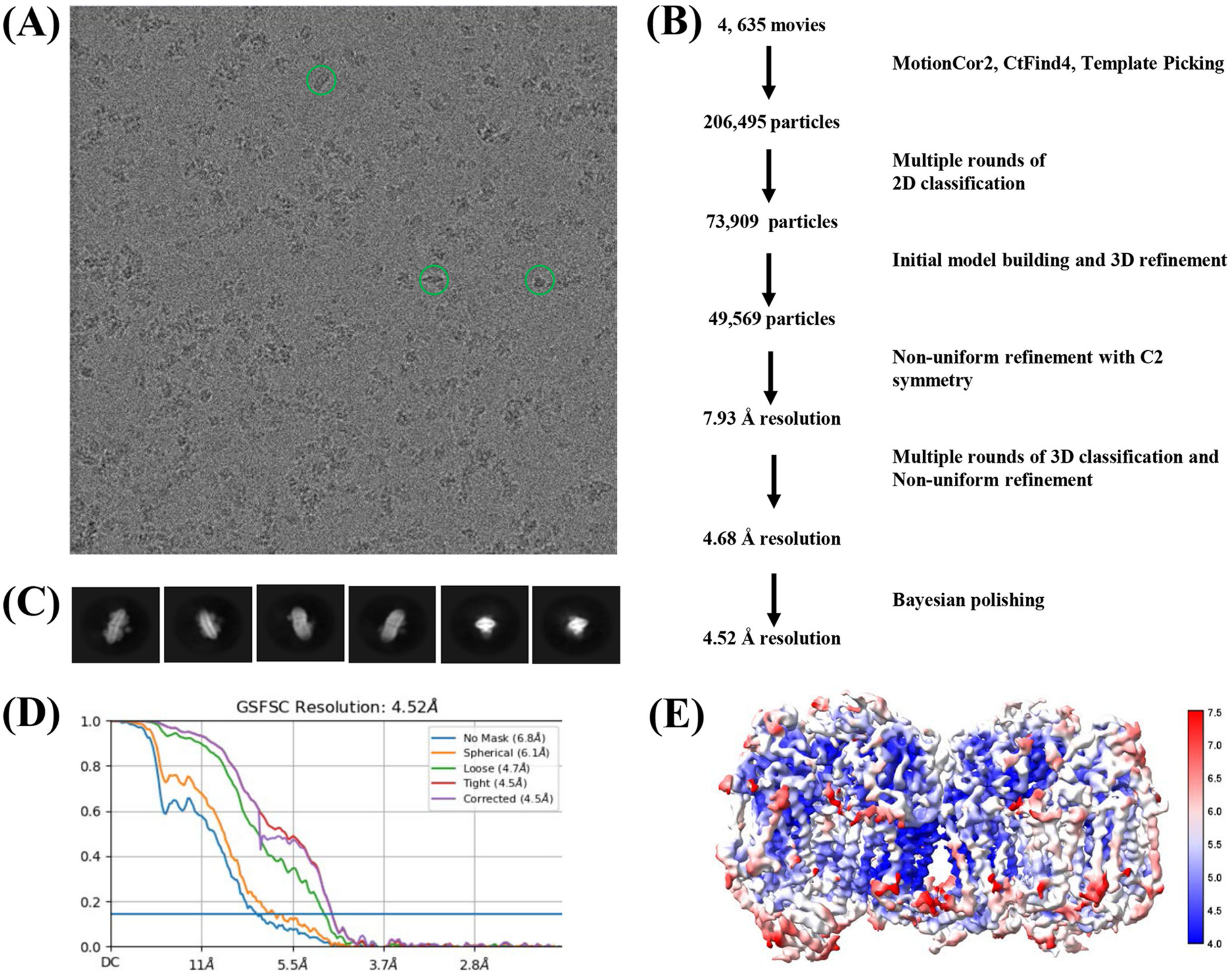

FIG 3 Cryo-EM data collection and processing. (A) Grid screening revealed the desired protein particles that resembled either a rod or eclipse shape. (B) Strategy of image analysis. (C) The acceptable 2D classes revealed rod- and eclipse-like structures. (D) A 4.6-Å structure was determined and further transferred to RELION v3.1 for Bayesian polishing, resulting in a final structure with a global 4.52-Å resolution. (E) The local resolution of the various regions was highlighted in a red-white-blue scale. The lowest resolution of 4 Å is represented by blue, and the highest resolution of 7 Å is represented by red.

was also capable to reduce oxygen to water, a 2,3-dimethyl-[1,4]naphthohydroquinone (DMNQ) oxidoreductase activity assay was carried out. The data shown in Fig. 2C demonstrate that the enzyme complex was able to reduce oxygen significantly. Titration of cyt-*bcc:aa*$_3$ with increasing concentrations of the substrate (2,3-dimethyl-[1,4]naphthohydroquinol [DMNQH$_2$]) gave a graded increase in Oxygen Consumption Rate (OCR) measurements with a calculated Michaelis constant (K_m) of about 75 μM and a catalytic rate constant (k_{cat}) of about 154 s^{-1} (Fig. 2D). These data enabled the catalytic efficiency (k_{cat}/K_m) to be estimated at 2 μM^{-1} s^{-1}. Based on this and to allow comparison of data published on other mycobacterial cyt-*bcc:aa*$_3$ oxygen consumption assays (7, 8), we used 100 μM DMNQH$_2$ for our downstream experiments.

Cryo-EM studies of recombinant *M. tuberculosis* cyt-*bcc:aa*$_3$. The recombinant *M. tuberculosis* cyt-*bcc:aa*$_3$ was monodispersed as visualized in cryo-EM images (Fig. 3A). In order to resolve a three-dimensional (3D) structure of the supercomplex, 4,635 movies were collected. Data processing was performed using cryoSPARC, as well as RELION v3.1 (Fig. 3A and B). Autopicking yielded 206,495 particles, which were classified into 100 2D classes, which provided 21 good classes (73,909 particles), that were selected for *ab initio* model building (Fig. 3C). The model was subjected to nonuniform refinement,

TABLE 1 Cryo-EM data acquisition and image processing of *M. tuberculosis* cyt-*bcc:aa*$_3$

Data acquisition and image processing	***M. tuberculosis* cyt-*bcc:aa*$_3$**
Data collection	
Electron microscope	Titan Krios
Camera	Gatan K2
Mode	Super-resolution counting
Voltage (kV)	300
Nominal magnification	130,000 ×
Calibrated physical pixel size (Å)	1.06
Exposure time (s)	9
Total exposure (e^-/Å^2)	40
No. of frames	40
Defocus range (μM)	1.0–2.0
Image processing	
Motion correction software	MotionCor2
CTF estimation software	CTFFind4
Particle selection software	cryoSPARC v3.3.1
2D classifications	cryoSPARC v3.3.1
3D classification and refinement software	RELION v3.1
Particle motion correction software	RELION v3.1

yielding a resolution of 4.63 Å, and further transferred to RELION v3.1 for Bayesian polishing. The resulting structure from RELION improved the resolution to 4.52 Å. Although the superoxide dismutase (sodC) was found to be associated with the *M. tuberculosis* cyt-*bcc:aa*$_3$ (see Fig. S1), the sodC resolution was low, which could be attributed to preferred orientation, leading to fewer particles displaying visible sodC. The final local resolution of the *M. tuberculosis* cyt-*bcc:aa*$_3$ density map (Fig. 3D and E) revealed an inner core of the cyt-*bcc* domain to have a higher resolution of closer to 4 Å compared to the exterior of the entire *M. tuberculosis* cyt-*bcc:aa*$_3$ complex. The model of the *M. tuberculosis* cyt-*bcc:aa*$_3$ was built into the map, using the structural model of the recently described mycobacterial cyt-*bcc:aa*$_3$ (PDB 7E1V) (7). The final structure, which was refined using Phenix and Coot, yielded a MolProbity score of 1.96. The cryo-EM map statistics and model statistics are presented in Tables 1 to 3. While the densities of most of the *M. tuberculosis* cyt-*bcc:aa*$_3$ subunits can be visualized clearly (see Fig. S2), the densities of subunits CtaI and CtaJ cannot be resolved properly in view of the low resolution (Table 3 and Fig. 3E).

Structure of the dimeric *M. tuberculosis* cyt-*bcc:aa*$_3$ supercomplex. The resolved *M. tuberculosis* cyt-*bcc:aa*$_3$ structure represents a dimer, with a C2 symmetry, consisting of the cyt-*bcc* and cyt-*aa*$_3$ domains (Fig. 4; see also Movie S1 in the supplemental material), with the core formed by the dimeric cyt-*bcc* units and the two cyt-*aa*$_3$ domains flanked at the outsides of the supercomplex. The structures of the three individual *M. tuberculosis* cyt-*bcc* subunits QcrC, QcrA, and QcrB are presented in Fig. S2A and include the cofactors heme b_H and b_L (QcrB), the iron-sulfur cluster (QcrA), and the hemes *c*I and *c*II of subunit QcrC. Figure S2B and C shows the determined structures of the *M. tuberculosis* cyt-*bcc:aa*$_3$ unit with the six subunits CtaC, CtaD, CtaE, CtaF, CtaI, and CtaJ. The cofactors of the catalytically active subunit CtaD (heme *a*, heme *a*$_3$) could

TABLE 2 Cryo-EM map statistics of resolved *M. tuberculosis* cyt-*bcc:aa*$_3$

Cryo-EM map parameter	***M. tuberculosis* cyt-*bcc:aa*$_3$**
No. of micrographs	4,635
No. of particle images selected	206,495
No. of particle images after clean-up	73,909
Particle images contributing to maps	49,569
Applies symmetry	C2
Applied box size (pixels)	500
Applied B-factor (Å^2)	142.2
Global resolution (FSC = 0.143, Å)	4.5

TABLE 3 Model building, model refinement, and model statistics for *M. tuberculosis* cyt-*bcc*:*aa*$_3$

EM model	***M. tuberculosis* cyt-*bcc*:*aa*$_3$**
Modeling software	Coot
Refinement software	Phenix
MolProbity score	1.96 (78th percentile)
EMRinger score	1.12
No. of residues	5,060
Clash score	11.03
CC (mask)	0.78
RMS bond	
Length (Å)	0.003
Angle (°)	0.742
Ramachandran	
Favored (%)	94.07
Outliers (%)	0.06
Rama-Z	0.98 ± 0.13
Ligands	Heme *a*, heme *b*, heme *c*, FeS

be clearly assigned (see Fig. S3), while the density for Cu$_B$ and Cu$_C$ in CtaD and Cu$_A$ in CtaC could not be determined.

The recent deposition of the analogous respiratory complex from *Corynebacterium glutamicum* (PDB 7QHO) (15) allowed for the comparison of the respiratory complexes between *C. glutamicum* and *M. tuberculosis*, which are both classified under the *Actinomycetota* phylum. The overall architectures between the two supercomplexes are similar, with both complexes sharing QcrA (root mean square deviation [RMSD] = 1.185 Å), QcrB (RMSD = 0.689 Å), QcrC (RMSD = 1.159 Å), CtaC (RMSD = 0.489 Å), CtaD (RMSD = 0.512 Å), CtaE (RMSD = 0.476 Å), and CtaF (RMSD = 0.669 Å) subunits with their respective RMSD values annotated. Notably, the superoxide dismutase observed in mycobacteria is absent and instead replaced with a soluble ThiX domain. The *C. glutamicum* supercomplex consists of additional subunits such as P29, P20, P12, P8, and P6 (15).

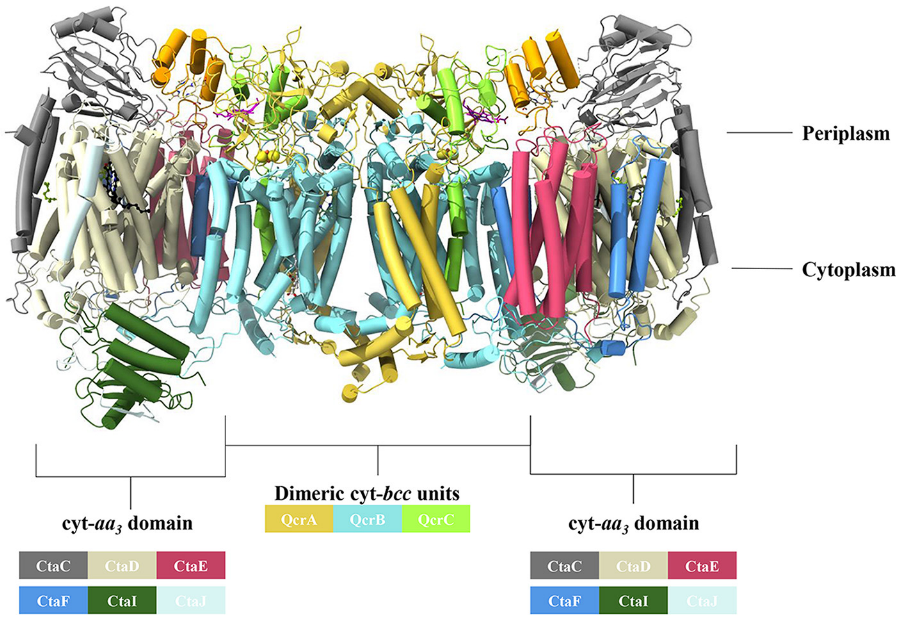

FIG 4 Dimeric cryo-EM structure of the resolved *M. tuberculosis* cyt-*bcc*:*aa*$_3$ oxidase. The cyt-*bcc* subunits in the structure consist of QcrC (green and orange), QcrA (gold), and QcrB (cyan). The cyt-*aa*$_3$ subunits constitute CtaC (gray), CtaJ (light blue), CtaD (cream), CtaE (magenta), CtaF (blue), and CtaI (dark green).

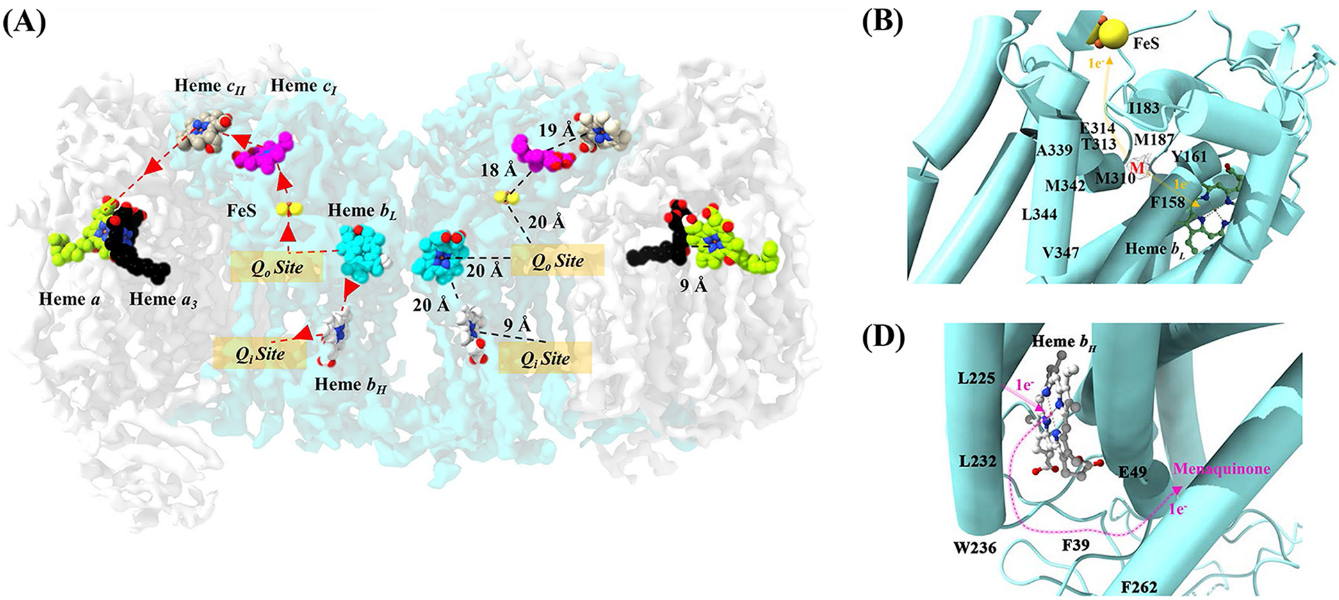

(C)

	Qo site								
Mtb	F158	Y161	I183	M187	T313	A339	M342	L344	V347
M. smegmatis	Y159	L175	I178	T179	W307	T308	D309	M337	

FIG 5 Electron transfer in resolved *M. tuberculosis* cyt-*bcc:aa*$_3$. (A) Electron transfer pathway. The left side of the dimer describes the electron transfer pathway, while the right side depicts the distances between the reaction centers. The binding of menaquinol to the Q_o site in QcrB initiates the electron transfer process. The first electron from menaquinol is transferred to FeS, which is ~20 Å from the Q_o site. The second electron from menaquinol is transferred to heme b_L, which is ~20 Å apart from the Q_o site and subsequently transferred to heme b_H. The electron from heme b_H is used to reduce a menaquinone bound at the Q_o site. FeS transfers its electron to the cytochrome *c* domain present in QcrC, which transfers the electron further to the cyt-*aa*$_3$ domain. The electrons are carried in the following order: from FeS to cyt-*c*I, cyt-*c*II, and Cu_A. The final electron transfer pathway occurs from Cu_A to heme *a* followed by Cu_B and heme a_3. The electrons at heme a_3 are used to reduce O_2 to H_2O. (B) Electron transfer in the Q_o site. The Q_o binding site with side chains interacting with menaquinol (M). The electron transfer pathway is illustrated with orange arrows. The binding of menaquinol results in the transfer of one electron to heme b_L and the other to FeS. (C) Amino acid residues that interact with menaquinol at the Q_o site revealed in the *M. tuberculosis* cyt-*bcc:aa*$_3$ and the *M. smegmatis* cyt-*bcc:aa*$_3$ structure. (D) Electron transfer in the Q_N site. The Q_i binding site with side chains is predicted to interact with menaquinone. The electron transfer pathway is illustrated by pink arrows. The electron, which originated from heme b_L, is transferred to heme b_H before being transferred to menaquinone in the Q_i site. The [2Fe-2S] and heme groups are shown as balls and sticks and are labeled in the figures. *Mtb*, *M. tuberculosis*.

Architecture of and electron transfer within the *M. tuberculosis* cyt-*bcc* domain. The oxidoreductase enzyme begins its cascade of events by binding of the electron donor menaquinol in the QcrB subunit of the *M. tuberculosis* cyt-*bcc* unit. The electron transfer pathway is initiated with the binding of menaquinol to the Q_o site in QcrB (Fig. 5A and B). Although the density obtained for the bound menaquinone tail was weak, the density for the head of the molecule was sufficient to highlight its binding within the Q_o site. The first electron from menaquinol can be transferred to the FeS cluster, which is ~20 Å away from the Q_o site of the presented *M. tuberculosis* QcrB structure (Fig. 5A and B). As shown in Fig. 5C, the *M. tuberculosis* residues F158, Y161, I183, M187, T313, A339, M342, L344, and V347 interacting with menaquinol differ from the ones of the *M. smegmatis* enzyme (Y158, L175, I178, T179, W307, T308, D309, and M337). Interestingly, substitution of the *M. tuberculosis* residue T313 to an alanine like in its *M. smegmatis* counterpart (T313A mutation) was associated with a high level of resistance to Q203 (6). The binding pocket of Q203 was recently revealed by Zhou et al. (7) with residues H375 of subunit QcrA and T313, as well as E314 of subunit QcrB mainly interacting with Q203. The strong anchoring interactions between the inhibitor at this site prevent menaquinol from binding, thus preventing electron transfer to both heme b_L and Fe-S, leading to the arrest of electron transfer within the complex.

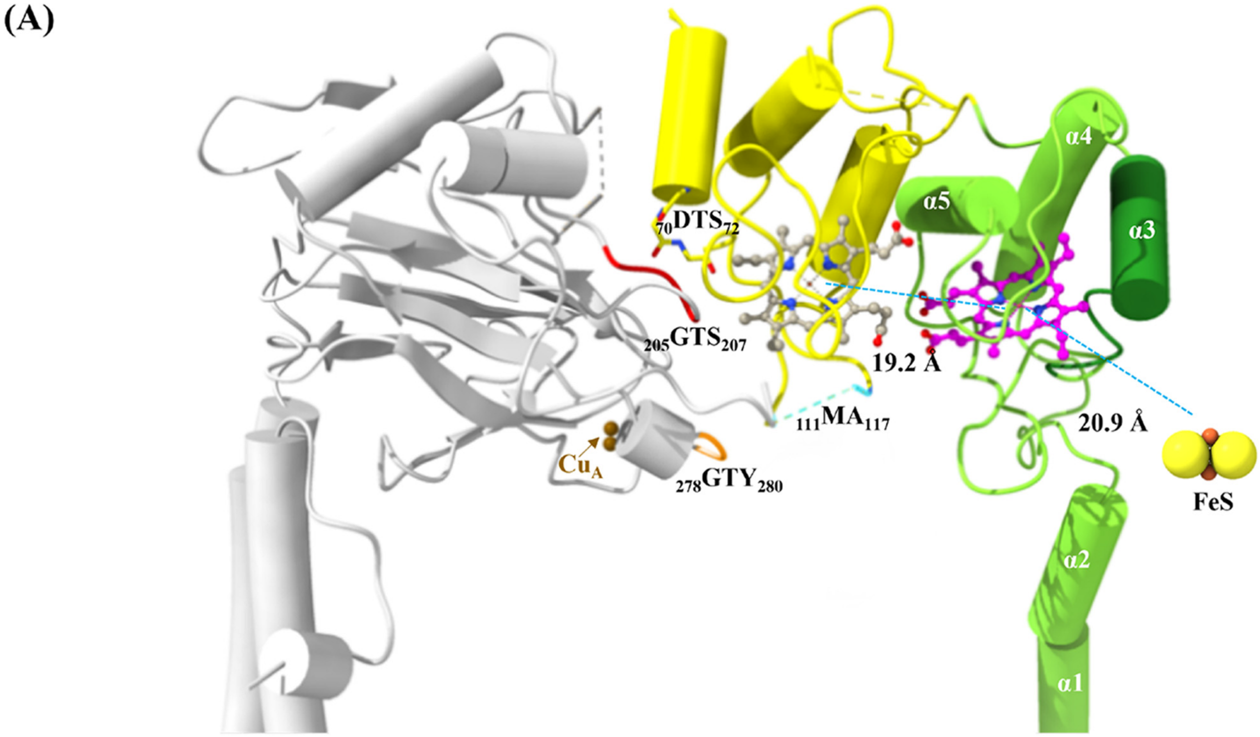

(B)

	QcrC Linker														
Mtb	V237	A238	T239	E240	A241	R242	Q243	P244	G245	G246	Y247	L248	L249	G250	G251	F252
M. smegmatis	E225	S226	A227	E228	T229	P230	S231	Y232	G233	G234	Y235	G236	L237	G238	G239	F240

FIG 6 *In silico* strategy to identify *M. tuberculosis* QcrC inhibitors. (A) Identification of region of interest in the QcrC functional domain. (B) Analysis of linker residue differences in QcrC between *M. tuberculosis* and *M. smegmatis*. *Mtb*, *M. tuberculosis*.

The second electron from menaquinol can be translocated to the low spin heme b_L of the *M. tuberculosis* QcrB, which is ~20 Å apart from the Q_o site (Fig. 5D). The electron from heme b_L is then transferred to the high spin heme b_H to reduce a menaquinone bound at the Q_i site (Fig. 5D). The heme b_L–heme b_H distance (~20 Å) is shorter compared to the heme b_L–FeS distance (~26 Å). The amino acids F39, E49, L225, L232 W236, and F262 are involved in the interaction with menaquinone, which becomes reduced to menaquinol in the Q_i site. While residues F34 and E44 of the *M. smegmatis* menaquinone binding site are similar, the latter differs by the two additional residues L47 and Y48, as well as the different amino acids L227, W231, F257, and S261.

Switching the cyt-*c*I*c*II head transfers electrons between the *bcc* and *aa*$_3$ domains. The cyt-*c*I*c*II head domains of both QcrCs, the counterpart of the soluble mitochondrial subunit *c*, are located between the cyt-*bcc* and cyt-*aa*$_3$ domains in the presented *M. tuberculosis* cyt-*bcc:aa*$_3$ dimer structure (Fig. 3 and 6), reflecting the so-called "closed state." In this closed state, the FeS cluster of QcrC is in ~18 Å proximity to heme c_I, while the second heme in cyt-*c*II is ~19 Å distant from cyt-*c*I (Fig. 6). Helix α3 of the cyt-c_{II} with its residues $_{70}$DTS$_{72}$ comes in close proximity (~10 Å) to the loop regions $_{205}$GTS$_{207}$ from CtaC, as well as the cyt-c_{II} loop $_{111}$MA$_{117}$ and the CtaC loop $_{278}$GTY$_{280}$ (~3.8 Å), providing structural bridges for the smooth electron transfer to Cu$_A$ inside subunit CtaC (Fig. 6). In comparison, the recently described *M. smegmatis* cyt-*bcc:aa*$_3$ dimer structure revealed a closed state, whereby the second cyt-*c*I*c*II head domain was in a so-called open conformation, in which the cyt-*c*I*c*II head domain interacts only with the cyt-*aa*$_3$ part (10). As a consequence, the FeS and cyt-*c*I distance increases to about 48 Å and

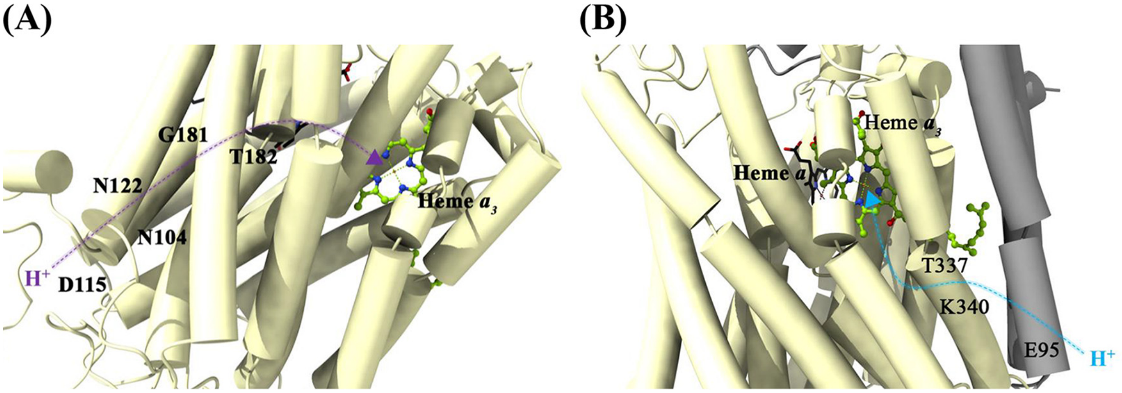

FIG 7 D- and K-proton pathways in *M. tuberculosis* cyt-*bcc:aa*$_3$. (A) The residues N104, D115, N122, G181, T182, and E266 of subunit CtaD constitute the D pathway. (B) Amino acids E95 (CtaC), T337 (CtaD), and K340 (CtaD) are assigned to the K pathway. The proton transfer direction and channels are shown in purple (D pathway) and blue (K pathway).

prevents electron transfer between the cyt-*bcc* and cyt-*aa*$_3$ domains (10). Switching from an open to a closed state is archived by the linker region of the QcrC transmembrane helix and the cyt-*c*lcII head domain. The *M. tuberculosis* linker $_{237}$VATEARQPGGYLLGGF$_{252}$ includes four glycine residues and one proline residue (see Fig. S2A), proposed to provide the flexibility for this region. Figure 6B shows the differences in amino acid composition of the *M. tuberculosis* linker compared to the *M. smegmatis* one.

Structural, mechanistic and assembly elements of the *M. tuberculosis* cyt-*aa*$_3$ units. The final electron transfer pathway occurs from Cu_A to heme *a*, Cu_B, and heme *a*$_3$ of the CtaC and CtaD subunits of the *M. tuberculosis* cyt-*aa*$_3$ domains (Fig. 5A). The electrons at heme *a*$_3$ are used for the reduction of O_2 to H_2O. The *M. tuberculosis* CtaD structure superimposes well with the *M. smegmatis* structure with an RMSD of 0.56 Å.

The reduction of O_2 inside the *M. tuberculosis* CtaD requires an uptake of eight protons from the negative side of the membrane. The K-proton pathway aids in the transfer of "substrate" protons to the catalytic site before O_2 binds to the catalytic Fe*a*$_3$/Cu_B site. The D-proton pathway aids in both the pumping of protons across the membrane and in transferring "substrate" protons to O_2. The amino acids N104, D115, N122, G181, T182, and E266 of subunit CtaD constitute the D pathway within the *M. tuberculosis* cyt-*aa*$_3$ domain (Fig. 7A), whereas the amino acids E95, T337, and K340 of subunit CtaC and CtaD, respectively, constitute the K pathway (Fig. 7B). The importance of this pathway is highlighted in the study, wherein the disruption of this pathway leads to growth impairment in *M. tuberculosis* (16).

The oxygen diffusion pathway in any mycobacterial *cytochrome aa*$_3$ has not been described thus far. Here, a prediction of the oxygen diffusion pathway within the *M. tuberculosis* CtaD is made based on the observations seen for the O_2 pathway in the *Thermus thermophilus* cytochrome *c* oxidase (17). The proposed oxygen diffusion pathway to *M. tuberculosis* heme *a*$_3$ has a Y-shaped channel with two entry points in subunit CtaD (see Fig. S4). The first entrance is flanked by amino acids A223 and L219, while the second entrance is flanked by residues F543 and L554. The two channels converge at F275 to continue to I270 and finally reach *M. tuberculosis* heme *a*$_3$.

Finally, *M. tuberculosis* CtaE, CtaF, CtaI, and CtaJ are described to function as assembly factors (see Fig. S2C). They are structurally similar to the *M. smegmatis* ones with an RMSD of 0.99 Å. CtaE consists of five transmembrane spanning α-helices (see Fig. S2C), while the 14.9-kDa *M. tuberculosis* CtaF is composed of four transmembrane spanning α-helices (α1, α2, α4, and α5) and the short helix α3, connected by random coiled elements (see Fig. S2C). The *M. tuberculosiss* CtaI subunit is located at the cytoplasmic site (Fig. 4), composed of an N-terminal tail, four α-helices, and three β-sheets (see Fig. S2C), while subunit CtaJ shows a transmembrane spanning α-helix, being linked to a terminal β-sheet via a long disordered region (Fig. 4; see also Fig. S2C).

Identification of a novel cyt-*c*I target and inhibitor. The CtaC and cyt-*c*lcII junction serves as an important interface orchestrating the transfer of electrons from the

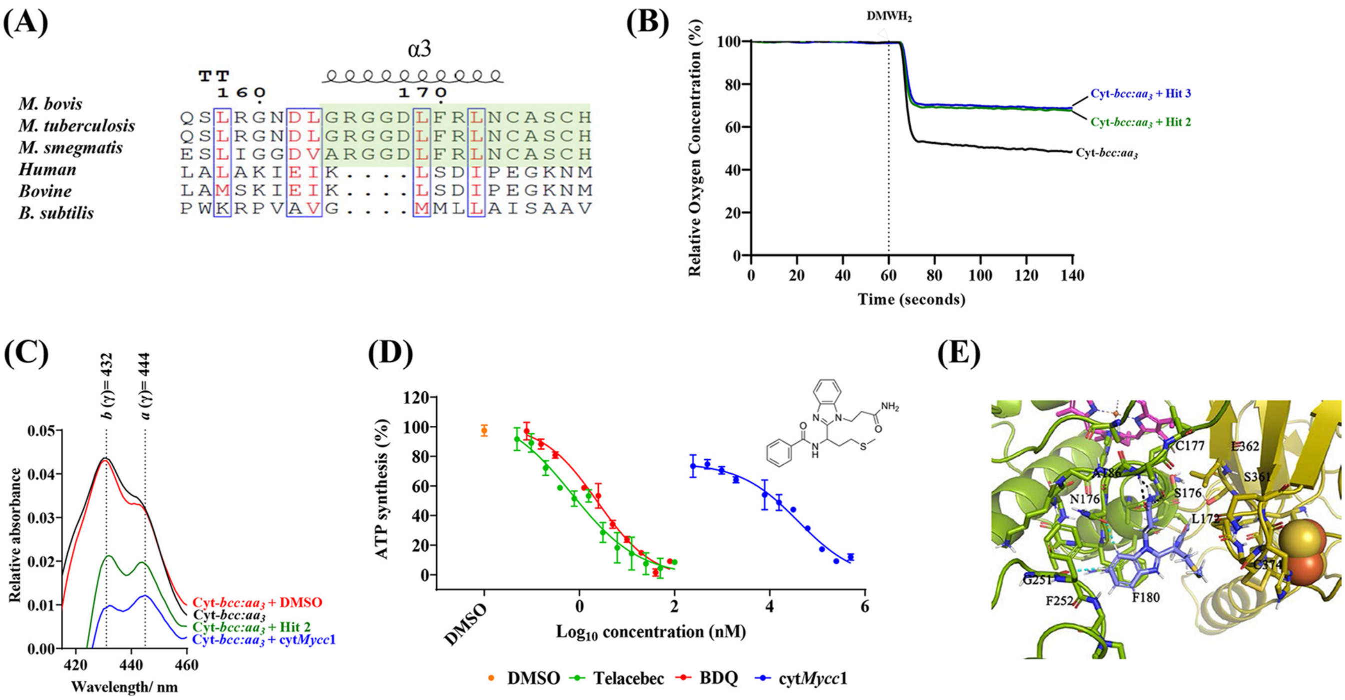

FIG 8 (A) Epitope sequence alignment between *M. bovis*, *M. tuberculosis*, *M. smegmatis*, humans, bovines, and *B. subtilis*. The region of interest is highlighted in green and found to be unique to mycobacteria. (B) Characterization of *in silico* screen hits 2 (green line) and 3 (blue line) in oxygen consumption assay with purified recombinant *M. tuberculosis* cyt-*bcc*:*aa*$_3$ (black line). In the presence of 2,3-dimethyl-[1,4]naphthohydroquinone, the supercomplex reduced oxygen levels by 50%, while hits 2 and 3 decreased respiration of the recombinant *M. tuberculosis* cyt-*bcc*:*aa*$_3$. (C) Effect of hits on electron transfer in the recombinant *M. tuberculosis* cyt-*bcc*:*aa*$_3$. cyt*Mycc*1 was incubated with recombinant *M. tuberculosis* cyt-*bcc*:*aa*$_3$ prior to oxidation with potassium ferricyanide. The conditions tested were compound free (black), DMSO (red), cytMycc1 (blue), or hit 2 (green). The heme *a* (444 nm) and heme *b* (432 nm) wavelengths showed drastic differences. All experiments were repeated at least once. (D) Effect of cyt*Mycc*1 on ATP synthesis of *M. smegmatis* IMVs. cyt*Mycc*1 (*blue circles*) had a starting concentration of 500 μM and was serially diluted by 2-fold. The starting concentration of Telacebec (red circles) and bedaquiline (BDQ; green circles) was 100 and 80 nM, respectively. The data points are expressed as means ± the standard deviations of triplicates from a representative experiment. The experiment was performed in triplicates and repeated more than once. (E) Binding pose of cyt*Mycc*1: the amide (NH$_2$) group on *N*-propionamide form H-bonding interactions (black dotted lines) with main chain carbonyl (CO) atoms of residues S176 and C177 and main chain NH atoms of A186 of QcrC. Benzimidazole has strong aromatic interactions with amino acids F180 and close contacts with N176 and G251. The propyl-thio-methyl fragment was in vicinity of QcrA (L362, S361, and C374) residues adjacent to the Fe-S cluster.

cyt-*bcc* to cyt-*aa*$_3$. The importance of subunit CtaC for growth (11) and the critical ability of cyt-cIcII head to switch between open / closed states, as observed in *M. smegmatis* cyt*bcc*:*aa*$_3$ (10), attracted attention to this site in *M. tuberculosis*. These distinct mycobacterial traits motivated us to pursue this cyt-cIcII interface for structure based ligand discovery in *M. tuberculosis*. Ligands that target this domain could potentially disturb interactions between the cyt-*bcc* and cyt-*aa*$_3$, disrupt the process of electron transfer to the catalytic center and thereby inhibit the oxidase functioning required for growth (11). While targeting the cyt-cII and CtaC interacting regions $_{70}$DTS$_{72}$-$_{205}$GTS$_{207}$ and the loops $_{111}$MA$_{117}$, as well a $_{278}$GTY$_{280}$ (Fig. 6A), may cause steric clashes with any compound during the switching mode of an open to a closed state, we focused on helix α3 of the subunit cyt-cI (Fig. 6A), since compound binding to that site would interrupt electron transfer between the FeS of QcrB and heme cI of the cyt-cyt-cIcII head and, thereby, the flow of electrons to the catalytic center in the *M. tuberculosis* cyt-*aa*$_3$ domain. Importantly, the sequence of helix α3 is unique to mycobacteria and does not exist in human or bovine mitochondrial or other bacterial cytochrome oxidase counterparts (Fig. 8A). Targeting this region may avoid undesirable interactions with potential enzymatic counterparts in the human host and evades off-target toxicity.

A virtual screening campaign (see Fig. S5) to identify novel chemical entities that could bind to the helix α3 residues was carried out. Our primary glide high-throughput virtual screening with 2 million compounds from the virtual enamine library (18) enabled us to segregate nonbinders from putative binders. Next, the ADMET (absorption, distribution, metabolism, excretion, and toxicity) properties of binder(s) subset poses were evaluated using the Qikprop tool to further exclude ligands with unfavorable solubility, clogP, and Human Ether-a-go-go-Related Gene (HERG) binding predictions. Only ligands (4,120) with a docking score below −5 kcal/mol and predicted to be non-hERG K^+ inhibitors (>-5 kcal/mol) were progressed to the next standard precision (SP) docking run. Ligand poses (*n* = 402) with an SP glide score of <-5 kcal/mol were taken further into the extra precision (XP) docking run (see the supplemental material). Finally, four hits that had favorable interactions with the amino acid residues surrounding the target region were selected for validation.

First, the effect of the four hits was tested by O_2 comsumption of the enzyme using DMNQ oxidoreductase activity. Figure 8B demonstrates a clear drop in O_2 comsumption of *M. tuberculosis* cyt-*bcc:aa*$_3$ in the presence of hits 2 and 3 after the addition of the electron donor DMNQH_2. Interestingly, the reduction profile of both hits is comparable to the one observed for the enzyme in the absence (addition of buffer) of DMNQH_2 (Fig. 2C), indicating their potency as an enzyme inhibitor.

To further test whether the drop in O_2 reduction within the heme *a* catalytic center is in line with the interruption of electron transfer to the O_2 reduction center, difference spectra of the supercomplex were measured with or without inhibitors (Fig. 8C). The difference spectrum (415 to 460 nm) of *M. tuberculosis* cyt-*bcc:aa*$_3$ energized with using 100 mM sodium dithionite ($Na_2S_2O_6$) demonstrated electron transfer, followed by the reduction of the cytochrome *bcc:aa*$_3$ hemes (*b* at 432 nm and *a* at 444). In comparison, the difference spectrum of *M. tuberculosis* cyt-*bcc:aa*$_3$ in the presence of sodium dithionite and hit 2 or hit 3 (*N*-(1-(1-(3-amino-3-oxopropyl)-1*H*-benzo[d]imidazol-2-yl)-3-(methylthio)propyl)benzamide, here called cyt*Mycc*1; Fig. 8C) displayed a drastic reduction of the peaks corresponding to the two hemes, confirming compound binding and inhibition of the electron transfer within the cytochrome *M. tuberculosis* cytochrome supercomplex. As a control, addition of dimethyl sulfoxide (DMSO; solvent) revealed no major change in the heme difference spectrum (Fig. 8C). The reduction of the heme *a* intensity supports the computational docking model where the disruption of the electron flow at the FeS and cyt-*c*I*c*II domain junction would inhibit electron flow at the O_2 reduction center. The reduction in intensity rather than the absence of a peak for heme *a* could imply that the compound has low binding affinity at the predicted epitope. The drop of heme *b* which was not initially predicted, could possibly be due to a feedback mechanism, by which the FeS cannot be regenerated to an electron acceptor for the next electron coming from the sodium dithionite/menaquinol, as the electron flow to the heme *c*I is interrupted. This may affect the electron transfer from menaquinol to the Q_i site, including heme b_L and b_H. At the moment, these scenarios can only be speculated and remain to be determined by mutational and/or cryo-EM efforts of an cyt*Mycc*1-*M. tuberculosis* cyt-*bcc:aa*$_3$ complex in future studies.

The ability of cyt*Mycc*1 to disrupt oxygen respiration in the complex was investigated further by adopting a dose-response strategy (see Fig. S7 in the supplemental material). In this experiment, the compound was serially diluted 2-fold from a starting concentration of 250 μM and subsequently incubated with the enzyme complex for 1 h before determining the effect of the compound on the rate of respiration. A graded dose-response was observed (see Fig. S7) with a 50% inhibitory concentration (IC_{50}) of 59 ± 3.7 μM. This further lends support to the ability of the hit compound cyt*Mycc*1 to target the *M. tuberculosis* cyt-*bcc:aa*$_3$.

Since switching of the opened and closed states of the cyt-*c*I*c*II head domain has only been demonstrated in the *M. smegmatis* cyt-*bcc:aa*$_3$ (10), we investigated whether inhibition of cyt-*bcc-aa*$_3$ by cyt*Mycc*1 may also reduce the process of oxidative phosphorylation within *M. smegmatis* inside outside vesicles (IMVs). As shown in Fig. 8D, cyt*Mycc*1 inhibited NADH-driven ATP synthesis of IMVs of parental *M. smegmatis* with an IC_{50} of 39.5 ± 0.2 μM, which is in the range of the IC_{50} value of the recombinant *M. tuberculosis* cyt-*bcc:aa*$_3$ described above. In comparison, cyt*Mycc*1 did not show a major effect on ATP formation of *Escherichia coli* IMVs, underlying its specificity, while the *E. coli* cytochrome b_{O3} inhibitor potassium cyanide (KCN) (19) significantly reduced

ATP synthesis levels by ~70% (see Fig. S8). Since *E. coli* IMVs contain also the NADH-dehydrogenase, succinate-dehydrogenases, cyt-*bd* oxidase, and the F-ATP synthase, the data underline also that cyt*Mycc1* does not nonspecifically inhibit the complexes of the entire *E. coli* oxidative phosphorylation pathway.

While cyt*Mycc*1 inhibited ATP formation on IMVs, no effect was observed in mycobacterial growth using *M. smegmatis* mc2 155 or *M. bovis* BCG, or in a whole-cell ATP assay (see Fig. S6). This may indicate that the compound does not reach the required concentration at the plasma membrane to exert antimicrobial activity. This is a well-known limitation of target-based approaches, as described before in the context of pantothenate kinase inhibitors, including problems such as limited cell envelope penetration, the presence of efflux pumps, and intrabacterial metabolism (20).

cyt*Mycc*1 interactions with mycobacterial subunits cyt-*c*I and QcrA. cyt*Mycc*I showed good docking XP score of −6.025 kcal/mol to subunit cyt-*c*I. The amide (NH_2) group on *N*-propionamide form H-bonding interactions with main chain carbonyl (CO) atoms of residues S176 and C177 and the main-chain NH atoms of A186 of cyt-*c*I (Fig. 8E). The 1*H*-benzo[d]imidazol-2-yl fragment was involved in strong aromatic π-π interactions with F180, as well as van der Waals contacts with N176 and G251 (Fig. 8E, blue hashed lines). The benzamide fragment was seated toward L172, whereas the methyl-thio-propyl fragment was in close vicinity to residues L362, S361, P373, and C374-C358 residues lining the Fe-S cluster of subunit QcrA (Fig. 8E). Taken together, cyt*Mycc*1 with its interactions to key residues such as S176 and C177 being in close proximity to residue H178, which is ligated to heme *c*I, could potentially hinder the electron transfer between the cyt-*bcc* and cyt-*aa*$_3$ domains and reduce cytochrome oxidase activity.

Conclusions. By establishing an expression system, the enzymatically active *M. tuberculosis* cyt-*bcc:aa*$_3$ could be produced and purified as a monodispersed enzyme complex, a prerequisite for the determination of the first entire *M. tuberculosis* cyt-*bcc:aa*$_3$ supercomplex structure. The resolved dimeric complex provides insights into the electron cascade from the substrate menaquinol via FeS, the cyt-c_Ic_{II} head to the catalytic center within subunit CtaD, as well as the electron transfer of the second electron of the substrate for the regeneration of menaquinone in the Q_i site. The proton pathways responsible for O_2 reduction and proton motive force, as well as oxygen entrance to the catalytic site, were discussed. So far, inhibitors targeting the mycobacterial cyt-*bcc:aa*$_3$ focused on the inhibition of the menaquinol binding site (5, 6). Insights into the closed confirmation of the *M. tuberculosis* cyt-*c*I*c*II head relative to subunit CtaC and the unique mycobacterial cyt-*c*I helix α3 paved the way for the identification of a new inhibitor target within the supercomplex and the novel inhibitor cyt*Mycc*1, which targets the mycobacterial cyt-*c*I and QcrA interface of cyt-*bcc:aa*$_3$ and affects electron transfer within the enzyme complex and finally, reduces ATP formation of the oxidative phosphorylation pathway within mycobacterial IMVs. The data presented underline that interrupting electron transfer within the mycobacterial supercomplex may open the door for novel mycobacterial cyt-*bcc:aa*$_3$ inhibitors.

MATERIALS AND METHODS

Generation of *M. bovis* BCG with genomic cyt-*bcc:aa*$_3$-FLAG/6×HIS tag. The mycobacterial shuttle vector pKM444 was first electroporated into wild-type (WT) *M. bovis* BCG. The resulting *M. bovis* BCG::pKM444 strain was selected on 7H10 complemented with oleic-acid-dextrose-catalase (OADC) plates, supplemented with 50 μg/mL kanamycin. Colonies were expended and grown to an optical density at 600 nm (OD_{600}) of 0.5 before induction with 500 ng/mL anhydrotetracycline for 24 h to express the Che9c phage RecT annealase and the Bxb1 phage integrase. The induced strain was washed in 0.05% Tween 80 at room temperature three times and finally resuspended to an OD_{600} of 100, before being coelectroporated with 200 ng of pKM 491 and 1 μg of targeting oligonucleotide 5′-CGA ACA ACG TGC CCT TGC CGC ACT GCG CGA ACA CCA GGA CAG CAT CAT GGG TTC GCC AGA CGG CGA GCA CGG TTT GTC TGG TCA ACC ACC GCG GTC TCA GTG GTG TAC GGT ACA AAC CTG ACC CGG CGA CGA CCC GGG TCG GCA CGA CCC GGG AAG GAA CCG GGC AAA TCA AGC ACA GCC CGG CGA CGA CC-3′. The electroporated cells were recovered overnight in 7H9-albumin-dextrose (ADS) culture broth medium. The recombinant strain was selected on 7H10-OADC plates, supplemented with 50 μg/mL hygromycin. The strain was validated by PCR with the forward primer 5′-CAC CAT TGA TGA CTC GAG TCT AGA GCA TG-3′ and the reverse primer 5′-ATG ATG GTG GTG GTG GTG GTG GTG-3′. The expression of the FLAG tag was validated by Western blotting.

Western blot validation of genomic FLAG tag. First, 1 mL of the culture strain (OD_{600} = 1) strain, containing the FLAG genomic tag, was sonicated for 1 min at 30% power using Bandelin Sonopuls (Bandelin, Berlin, Germany) for five cycles. The sonicated sample was centrifuged at 12,000 rpm. The supernatant was applied to a 12% SDS gel and transferred to a nitrocellulose membrane using a semidry transfer apparatus according to the manufacturer's protocols (Carl Roth, Karlsruhe, Germany). After blocking with 3% gelatin in a TBSN-Tween buffer (20 mM Tris-HCl [pH 7.5], 500 mM NaCl, 0.02% NaN_3, and 0.05% Tween 20) for 1 h at room temperature, the membrane was washed with 1% gelatin in TBSN-Tween for 3 × 10 min. Afterward, the membranes were incubated with a rabbit anti-FLAG HRP-conjugated antibodies against the FLAG tag (Abcam, Cambridge, United Kingdom) diluted (1:2,000) with 1% gelatin TBSN-Tween 20 for 1 h at room temperature, followed by three washing steps (15 min) with TBSN-Tween 20 buffer. The antibodies were detected using SuperSignal West Pico Plus chemiluminescent substrate according to the manufacturer's protocol (Thermo Fisher Scientific, Waltham, MA).

Purification of *M. tuberculosis* cyt-*bcc:aa*$_3$. The strain containing the genomic tag was grown in 7H9-ADS-glycerol medium until reaching an OD_{600} of 2.0 to 2.5. Cell pellets were harvested and stored in −80°C. Then, 10 g of cell pellets was dissolved in 100 mL of buffer A (20 mM MOPS [pH 7.4], 100 mM NaCl, 2 mM Pefabloc, 1 mM PMSF, 10% glycerol) and briefly sonicated in ice to ensure complete resuspension. Cell lysis was achieved by three passes through a microfluidizer (Microfluidics, Newton, MA) at 4°C and 1.2E+8 Pa. The lysate was centrifuged at 12,000 rpm for 20 min to remove cell debris and unlysed cells. The resulting supernatant was centrifuged at 36,900 rpm for 1 h in a P50AT2 rotor (Hitachi Himac Ultracentrifuge; Eppendorf Himac Technologies Co., Ltd., Japan). The membrane pellets from the previous step were resuspended in buffer B (20 mM MOPS [pH 7.4], 100 mM NaCl, 2 mM Pefabloc, 1 mM PMSF, 1% [wt/vol] DDM, 5% glycerol). The mixture was stirred for 1 h at 4°C on a rotating wheel. After solubilization with the detergent, the mixture was centrifuged at 18,000 rpm for 30 min at 4°C. The supernatant was allowed to equilibrate with 1 mL of FLAG beads for 1 h; the resin was then washed with buffer C (20 mM MOPS [pH 7.4], 100 mM NaCl, 2 mM Pefabloc, 1 mM PMSF, 0.1% [wt/vol] DDM). The protein was eluted with buffer D (20 mM MOPS [pH 7.4], 100 mM NaCl, 2 mM Pefabloc, 1 mM PMSF, 0.1% [vol/wt] DDM, 100 μg/mL). Protein samples that were collected during the course of the experiment were analyzed using 12% SDS-PAGE.

Heme absorbance spectra of purified *M. tuberculosis* cyt-*bcc:aa*$_3$. The spectra were analyzed with an Amersham Biosciences Ultrospec 2100 Pro-UV-Visible absorption spectroscopy (Amersham, Piscataway, NJ). The spectra were recorded from wavelengths of 400 to 700 nm. The purified *M. tuberculosis* cyt *bcc:aa*$_3$ at a concentration of 1 mg/mL was oxidized with 100 μM potassium ferricyanide. The oxidized UV spectra were subsequently recorded. The sample was reduced using 100 mM sodium dithionite. The reduced UV spectrum was recorded promptly. The difference spectra were then obtained by subtracting the absorbance value of the reduced state from that of the oxidized state.

2,3-Dimethyl-1,4-naphthoquinol oxygen consumption assay. DMNQ was purchased from Enamine, Cincinnati, OH. Next, 20 mM DMNQ was prepared in 1 mL of ethanol containing 6 mM HCl. The DMNQ solution was reduced with a few grains of sodium borohydride ($NaBH_4$) in an ice bath. Then, 10 μL of 12 N HCl was used to quench the reaction. This reaction resulted in the formation of $DMNQH_2$.

The oxygen consumption assay was performed based on published protocols (7, 8). Briefly, the purified *M. tuberculosis* cyt-*bcc:aa*$_3$ was resuspended in 500 μL of reaction buffer (20 mM MOPS [pH 7.4], 100 mM NaCl, 0.01% DDM) to a final concentration of 65 nM. Next, 5 μL of $DMNQH_2$ was added to the mixture to yield a final concentration of 25 μM. This initiated respiration within the supercomplex, which was monitored by a Clark-type oxygen electrode (Oxytherm$^+$, Hansatech, Pentney, United Kingdom). The oxygen consumption curve was plotted using GraphPad Prime 8.0 software (21).

Cryo-EM. The purified *M. tuberculosis* cyt-*bcc:aa*$_3$ was concentrated to 9 mg/mL. Portions (4 μL) of the sample were applied to glow-discharged Quantifoil R1.2/1.3 holey carbon grids. The grids were blotted for 2 s at 100% humidity and 4°C and plunge-frozen using a FEI Vitrobot Mark IV (Thermo Fisher Scientific). Images were taken using an FEI Titan Krios electron microscope operating at 300 kV with a K2 Summit detector (Gatan, Pleasanton, CA) at a magnification of ×130,000. Images were recorded in super-resolution mode. Automated single-particle data acquisition was performed using EPU software. A defocus range of 1.0 to 2.0 μm was implemented. Movies were collected at 40 frames per stack with an exposure time of 9 s. The total dose was set at 40 $e^-/Å^2$. Motion correction was performed using MotionCor2 and CTF refinement was performed using CTFFind4 (22, 23). The initial data processing was performed on CryoSPARC and RELION v3.1 (24, 25). Structure refinement was done using COOT and Phenix software (26, 27).

Data availability. All relevant data are available from the authors. Structural data that supports the findings of this study are openly available from the Protein Data Bank (https://www.rcsb.org; PDB ID 8HCR) and the EM Data Bank (https://www.ebi.ac.uk/emdb/; EMDB ID EMD-34664).

SUPPLEMENTAL MATERIAL

Supplemental material is available online only.

SUPPLEMENTAL FILE 1, PDF file, 1.3 MB.

SUPPLEMENTAL FILE 2, MOV file, 15.6 MB.

ACKNOWLEDGMENTS

This study was supported by National Research Foundation (NRF) Singapore, NRF Competitive Research Program (CRP), grants NRF-CRP18-2017-01 and NRF-CRP27-2021-

0002. V.M. acknowledges a NTU Research Scholarship. C.-F.W.'s Ph.D. scholarship was funded by an NRF CRP grant (award NRF-CRP18-2017-01). We also acknowledge the use of the EM facility at the NTU Institute of Structural Biology.

V.M., C.-F.W., A.H., K.P., and G.G. designed the experiments. V.M., C.-F.W., A.H., K.P., and G.G. conducted the formal analysis. V.M., C.-F.W., and A.H. performed investigations. V.M., A.H., K.P., and G.G. wrote the original draft. All authors contributed to the writing (both review and editing). K.P. and G.G. obtained funding.

We declare no competing interests.

REFERENCES

1. Rao SPS, Alonso S, Rand L, Dick T, Pethe K. 2008. The proton motive force is required for maintaining ATP homeostasis and viability of hypoxic, nonreplicating *Mycobacterium tuberculosis*. Proc Natl Acad Sci U S A 105:11945–11950. https://doi.org/10.1073/pnas.0711697105.
2. Koul A, Vranckx L, Dendouga N, Balemans W, Van den Wyngaert I, Vergauwen K, Göhlmann HWH, Willebrords R, Poncelet A, Guillemont J, Bald D, Andries K. 2008. Diarylquinolines are bactericidal for dormant mycobacteria as a result of disturbed ATP homeostasis. J Biol Chem 283:25273–25280. https://doi.org/10.1074/jbc.M803899200.
3. Cook GM, Hards K, Dunn E, Heikal A, Nakatani Y, Greening C, Crick DC, Fontes FL, Pethe K, Hasenoehrl E, Berney M. 2017. Oxidative phosphorylation as a target space for tuberculosis: success, caution, and future directions. Microbiol Spectr 5:5.3.14. https://doi.org/10.1128/microbiolspec.TBTB2-0014-2016.
4. Kalia NP, Hasenoehrl EJ, Ab Rahman NB, Koh VH, Ang MLT, Sajorda DR, Hards K, Grüber G, Alonso S, Cook GM, Berney M, Pethe K. 2017. Exploiting the synthetic lethality between terminal respiratory oxidases to kill *Mycobacterium tuberculosis* and clear host infection. Proc Natl Acad Sci U S A 114:7426–7431. https://doi.org/10.1073/pnas.1706139114.
5. Tang J, Wang B, Wu T, Wan J, Tu Z, Njire M, Wan B, Franzblauc SG, Zhang T, Lu X, Ding K. 2015. Design, synthesis, and biological evaluation of pyrazolo [1,5-*a*]pyridine-3-carboxamides as novel antitubercular agents. ACS Med Chem Lett 6:814–818. https://doi.org/10.1021/acsmedchemlett.5b00176.
6. Pethe K, Bifani P, Jang J, Kang S, Park S, Ahn S, Jiricek J, Jung J, Jeon HK, Cechetto J, Christophe T, Lee H, Kempf M, Jackson M, Lenaerts AJ, Pham H, Jones V, Seo MJ, Kim YM, Seo M, Seo JJ, Park D, Ko Y, Choi I, Kim R, Kim SY, Lim S, Yim S-A, Nam J, Kang H, Kwon H, et al. 2013. Discovery of Q203, a potent clinical candidate for the treatment of tuberculosis. Nat Med 19:1157–1160. https://doi.org/10.1038/nm.3262.
7. Zhou S, Wang W, Zhou X, Zhang Y, Lai Y, Tang Y, Xu J, Li D, Lin J, Yang X, Ran T, Chen H, Guddat LW, Wang Q, Gao Y, Rao Z, Gong H. 2021. Structure of *Mycobacterium tuberculosis* cytochrome bcc in complex with Q203 and TB47, two anti-TB drug candidates. Elife 10:e69418. https://doi.org/10.7554/eLife.69418.
8. Yanofsky DJ, Di Trani JM, Król S, Abdelaziz R, Bueler SA, Imming P, Brzezinski P, Rubinstein JL. 2021. Structure of mycobacterial CIII2CIV2 respiratory supercomplex bound to the tuberculosis drug candidate Telacebec (Q203). Elife 10:e71959. https://doi.org/10.7554/eLife.71959.
9. Gong H, Li J, Xu A, Tang Y, Ji W, Gao R, Wang S, Yu L, Tian C, Li J, Yen H-Y, Lam SM, Shui G, Yang X, Sun Y, Li X, Jia M, Yang C, Jiang B, Lou Z, Robinson CV, Wong L-L, Guddat LW, Sun F, Wang Q, Rao Z. 2018. An electron transfer path connects subunits of a mycobacterial respiratory supercomplex. Science 362:eaat8923. https://doi.org/10.1126/science.aat8923.
10. Wiseman B, Nitharwal RG, Fedotovskaya O, Schäfer J, Guo H, Kuang Q, Benlekbir S, Sjöstrand D, Ädelroth P, Rubinstein JL, Brzezinski P, Högbom M. 2018. Structure of a functional obligate complex III2IV2 respiratory supercomplex from *Mycobacterium smegmatis*. Nat Struct Mol Biol 25:1128–1136. https://doi.org/10.1038/s41594-018-0160-3.
11. Matsoso LG, Kana BD, Crellin PK, Lea-Smith DJ, Pelosi A, Powell D, Dawes SS, Rubin H, Coppel RL, Mizrahi V. 2005. Function of the cytochrome bc_1:aa_3 branch of the respiratory network in mycobacteria and network adaptation occurring in response to its disruption. J Bacteriol 187:6300–6308. https://doi.org/10.1128/JB.187.18.6300-6308.2005.
12. Saw WG, Wong CF, Dick T, Grüber G. 2020. Overexpression, purification, and enzymatic and microscopic characterization of recombinant mycobacterial F-ATP synthase. Biochem Biophys Res Commun 522:374–380. https://doi.org/10.1016/j.bbrc.2019.11.098.
13. Zhang AT, Montgomery MG, Leslie AGW, Cook GM, Walker JE. 2019. The structure of the catalytic domain of the ATP synthase from *Mycobacterium smegmatis* is a target for developing antitubercular drugs. Proc Natl Acad Sci U S A 116:4206–4211. https://doi.org/10.1073/pnas.1817615116.
14. Murphy KC, Nelson SJ, Nambi S, Papavinasasundaram K, Baer CE, Sassetti CM. 2018. ORBIT: a new paradigm for genetic engineering of mycobacterial chromosomes. mBio 9:e01467-18. https://doi.org/10.1128/mBio.01467-18.
15. Kao WC, Ortmann de Percin Northumberland C, Cheng TC, Ortiz J, Durand A, von Loeffelholz O, Schilling O, Biniossek ML, Klaholz BP, Hunte C. 2022. Structural basis for safe and efficient energy conversion in a respiratory supercomplex. Nat Commun 13:545. https://doi.org/10.1038/s41467-022-28179-x.
16. Beites T, O'Brien K, Tiwari D, Engelhart CA, Walters S, Andrews J, Yang H-J, Sutphen ML, Weiner DM, Dayao EK, Zimmerman M, Prideaux B, Desai PV, Masquelin T, Via LE, Dartois V, Boshoff HI, Barry CE, Ehrt S, Schnappinger D. 2019. Plasticity of the *Mycobacterium tuberculosis* respiratory chain and its impact on tuberculosis drug development. Nat Commun 10:4970. https://doi.org/10.1038/s41467-019-12956-2.
17. Zhu G, Zeng H, Zhang S, Juli J, Tai L, Zhang D, Pang X, Zhang Y, Lam SM, Zhu Y, Peng G, Michel H, Sun F. 2021. The unusual homodimer of a heme-copper terminal oxidase allows itself to utilize two electron donors. Angew Chem Int Ed Engl 60:13323–13330. https://doi.org/10.1002/anie.202016785.
18. Irwin JJ, Shoichet BK. 2005. ZINC: a free database of commercially available compounds for virtual screening. J Chem Inf Model 45:177–182. https://doi.org/10.1021/ci049714+.
19. Asseri AH, Godoy-Hernandez A, Goojani HG, Lill H, Sakamoto J, McMillan DGG, Bald D. 2021. Cardiolipin enhances the enzymatic activity of cytochrome *bd* and cytochrome bo_3 solubilized in dodecyl-maltoside. Sci Rep 11:8006. https://doi.org/10.1038/s41598-021-87354-0.
20. Barry CE, III, Boshoff HI, Dartois V, Dick T, Ehrt S, Flynn J, Schnappinger D, Wilkinson RJ, Young D. 2009. The spectrum of latent tuberculosis: rethinking the biology and intervention strategies. Nat Rev Microbiol 7:845–855. https://doi.org/10.1038/nrmicro2236.
21. Motulsky H, Christopoulos A. 2003. Fitting models to biological data using linear and nonlinear regression: a practical guide to curve fitting. GraphPad Software, Inc, San Diego, CA.
22. Zheng SQ, Palovcak E, Armache JP, Verba KA, Cheng Y, Agard DA. 2017. MotionCor2: anisotropic correction of beam-induced motion for improved cryo-electron microscopy. Nat Methods 14:331–332. https://doi.org/10.1038/nmeth.4193.
23. Rohou A, Grigorieff N. 2015. CTFFIND4: fast and accurate defocus estimation from electron micrographs. J Struct Biol 192:216–221. https://doi.org/10.1016/j.jsb.2015.08.008.
24. Punjani A, Rubinstein JL, Fleet DJ, Brubaker MA. 2017. cryoSPARC: algorithms for rapid unsupervised cryo-EM structure determination. Nat Methods 14:290–296. https://doi.org/10.1038/nmeth.4169.
25. Zivanov J, Nakane T, Forsberg BO, Kimanius D, Hagen WJH, Lindahl E, Scheres SHW. 2018. New tools for automated high-resolution cryo-EM structure determination in RELION-3. Elife 7:e42166. https://doi.org/10.7554/eLife.42166.
26. Noble M, Perrakis A. 2004. Model building and refinement. Acta Crystallographica Section D 60.
27. Liebschner D, Afonine PV, Baker ML, Bunkoczi G, Chen VB, Croll TI, Hintze B, Hung L-W, Jain S, McCoy AJ, Moriarty NW, Oeffner RD, Poon BK, Prisant MG, Read RJ, Richardson JS, Richardson DC, Sammito MD, Sobolev OV, Stockwell DH, Terwilliger TC, Urzhumtsev AG, Videau LL, Williams CJ, Adams PD. 2019. Macromolecular structure determination using X-rays, neutrons and electrons: recent developments in Phenix. Acta Crystallogr D Struct Biol 75:861–877. https://doi.org/10.1107/S2059798319011471.